Communication

A GEO-GEO Stereo Observation of Diurnal Cloud Variations over the Eastern Pacific

Dong L. Wu [1,*], James L. Carr [2], Mariel D. Friberg [1,3], Tyler C. Summers [4], Jae N. Lee [5] and Ákos Horváth [6]

1 NASA Goddard Space Flight Center, Greenbelt, MD 20771, USA
2 Carr Astronautics, Greenbelt, MD 20770, USA; jcarr@carrastro.com
3 Earth System Science Interdisciplinary Center (ESSIC), University of Maryland, College Park, MD 20740, USA
4 Science Systems and Applications Inc., Lanham, MD 20706, USA; tyler.summers@nasa.gov
5 Goddard Earth Sciences Technology and Research (GESTAR-II), University of Maryland, Baltimore County, Baltimore, MD 21228, USA; jae.n.lee@nasa.gov
6 Meteorological Institute, Universität Hamburg, 20146 Hamburg, Germany; akos.horvath@uni-hamburg.de
* Correspondence: dong.l.wu@nasa.gov

Abstract: Fast atmospheric processes such as deep convection and severe storms are challenging to observe and understand without adequate spatiotemporal sampling. Geostationary (GEO) imaging has the advantage of tracking these fast processes continuously at a cadence of the 10 min global and 1 min mesoscale from thermal infrared (TIR) channels. More importantly, the newly-available GEO-GEO stereo observations from our 3D-Wind algorithm provide more accurate height assignment for atmospheric motion vectors (AMVs) than those from conventional TIR methods. Unlike the radiometric methods, the stereo height is insensitive to radiometric TIR calibration of satellite sensors and can assign the feature height correctly under complex situation (e.g., multi-layer clouds and atmospheric inversion). This paper shows a case study from continuous GEO-GEO stereo observations over the Eastern Pacific during 1–5 February 2023, to highlight diurnal variations of clouds and dynamics in the planetary boundary layer (PBL), altocumulus/congestus, convective outflow and tropical tropopause layer (TTL). Because of their good vertical resolution, the stereo observations often show a wind shear in these cloud layers. As an example, the stereo winds reveal the classic Ekman spiral in marine PBL dynamics with a clockwise (counterclockwise) wind direction change with height in the Northern (Southern) Hemisphere subtropics. Over the Southeastern Pacific, the stereo cloud observations show a clear diurnal variation in the closed-to-open cell transition in the PBL and evidence of precipitation at a lower level from broken stratocumulus clouds.

Keywords: stereo height; atmospheric motion vector; height assignment; clouds; planetary boundary layer; congestus; Ekman spiral; diurnal cycle; wind shear

1. Introduction

Atmospheric wind measurements are critical for weather and air quality forecasts. It is atmospheric winds that transport energy, water, carbon, aerosol, and trace gases through the air. Winds play a fundamental role in cloud formation and precipitation processes that drive the energy and water cycles in Earth's climate system. Realistic winds derived from regional and global models also have a direct impact on the fidelity of their skills in predicting future climate changes [1]. Observation of winds in the lower atmosphere, especially in the planetary boundary layer (PBL) that is typically at heights less than 2 km, has been a great challenge for remote sensing from space. Wind data remain a high priority of global observations for improving forecasts of adverse weather systems, air pollution outbreaks, renewable wind energy applications, and for transport and distribution of global water and carbon in the Earth system.

Satellite stereo-photogrammetry is a well-known technique to determine cloud top height (or stereo height) in addition to cloud motion [2–9]. Imaging cloud features from

multiple view angles usually requires a horizontal pixel resolution higher than 1 km for an appreciable vertical resolution. The stereo technique overcomes some of the limitations in other height-registration methods for atmospheric motion vectors (AMVs), such as CO_2 slicing [10]. Compared to the AMV height determined from infrared (IR) techniques, the stereo technique is less sensitive to atmospheric thermal structures and surface types that may pose a challenge for IR-based height assignment. Atmospheric temperature inversions and cold surfaces often cause large height errors due to ambiguity in the IR solution.

Recent studies have demonstrated that stereo observations from satellite imagers on different geostationary (GEO) and low Earth orbit (LEO) platforms can produce 3D regional AMVs with an accurate height assignment [11–15]. Derived from tracking cloud and moisture features in motion, AMVs have proven to be very valuable for weather forecasts [16,17]. A stereo wind observation can be obtained by pairing GEO-GEO, GEO-LEO and LEO-LEO imagers at different vantage points from space. No synchronization in the observations is required as long as the sampling time is taken into account in the retrieval algorithm. Compared to conventional AMV measurements, which are derived from sensors on a single platform, the stereo technique produces AMVs with a better height assignment and helps to reduce the speed bias and mean vector difference against rawinsonds [13]. The accuracy of Image Navigation and Registration (INR) is critical for stereo observation from a far distance, and modern observing systems such as the Geostationary Operational Environmental Satellite R-series (GOES-R) Advanced Baseline Imager (ABI) have geo-registration accuracy down to a few tenths of a pixel [18,19]. The better height assignment for AMVs is critical for studying the processes in the lower atmosphere and PBL where some of the stratified layers are as narrow as 1 km. Because of the improved height assignment, it was shown that assimilating the GEO-GEO stereo winds produced significant positive impacts on forecast error reductions in the U.S. Navy's global numerical weather prediction system that is based on NAVGEN (Navy Global Environmental Model) [20]. Particularly in the PBL, there are considerably large impacts from the stereo wind measurements.

Several new science applications have emerged from the recent availability of satellite stereo observations. Carr et al. [2020] showed that the GEO-GEO stereo observations are able to continuously track adverse weather systems such as Tropical Storm Imelda (2019), Hurricane Hanna (2020), and California Creak Fire (2020), and reveal structural evolution and diurnal variations of cloud dynamics. Horváth et al. [21] used the 3D-Wind stereo measurements to study the classic Kármán vortex formed in the stratocumulus-capped wake over the lee side of Guadalupe Island. Using the pairing between Himawari-8 (H8) and GOES-17 (G17), Carr et al. [14] applied the 3D-Wind algorithm to the historical eruption of Hunga Tonga-Hunga Ha'apai (HTHH) volcano and reported a record 55 km plume height and massive outflows in the stratosphere. Extending the 3D-Wind algorithm to multi-LEO pairing, Carr et al. [15] demonstrated a science application of stereo observations for polar atmospheric circulation and nighttime cloud identification.

To continue the exploration with the stereo observations from space, in this study we applied the research 3D-Wind algorithm to the full-disk (FD) GOES-16 (G16) and GOES-18 (G18) pairing and processed all overlapped 11.2 μm (C14) measurements from 1–5 February 2023, which produced AMVs and cloud heights at a refresh rate of 10 min for the full disk, 5 min over the CONUS (Continental United States), and 1 min over a mesoscale domain. This unique data set allows us to study the diurnal variation, cloud lifecycle, and atmospheric dynamics in detail over these regions. By tracking broken clouds from different places within a mesoscale domain (e.g., ~100 km), the stereo algorithm can extract winds from different altitudes in the domain, providing a 3D representation of the regional dynamics. Because of the improved height assignment of AMVs from the stereo technique, the 10 min stereo AMVs and their global coverage will be a great benefit to the numerical weather prediction (NWP) community as well for process studies on cloud dynamics.

The objective of this study is to demonstrate a capability of the 3D-Wind algorithm in observing the regional AMVs and their diurnal variations in the lower troposphere

where the vertical resolution is critical for sheared flows. In this paper we evaluate the derived AMV variations and cloud statistics over the mesoscale domains such that the measurements have samples from different altitudes on an hourly basis. In a 5-day full-disk retrieval test with the 3D-Wind algorithm, the continuous coverage from the G16–G18 IR bands helps to separate between localized repeatable diurnal variations and transient weather systems that contain various oceanic cloud types. The study also features Ekman spirals in the mesoscale PBL dynamics that have not been observed by previous remote sensing techniques from GEO.

2. Data and Method

GEO stereo observations with the improved INR performance (i.e., geometric accuracy and stability) offer a spatiotemporal coverage needed for studying fast processes such as convective clouds from strong storms, the pyrocumulus overshot from intense wildfires, and unexpected eruptions like the HTHH. Although the stereo observations are not fully global, as shown in Figure 1, the GEO-ring constellation begins to provide a wide longitudinal coverage, which allows stereo pairing between adjacent satellites. Notably, the 3D-Wind algorithm has been developed for the pairings between H8/H9 and GOES-West (G17/G18) and GOES-West (G17/G18) and GOES-East (G16). More recently, the algorithm has been demonstrated for H8–GK2A pairing [22] and triple GEO (G16–G17–G18) stereo [23]. The future 3D-Wind developments include the pairing between GOES-East and the newly launched MTG-l1 (Meteosat Third Generation—Imaging 1). The Flexible Combined Imager (FCI) on MTG-l1 also has a modernized INR system and a set of spectral channels similar to the GOES-R series, which allows high-quality stereo wind retrievals from pairing with GOES-East.
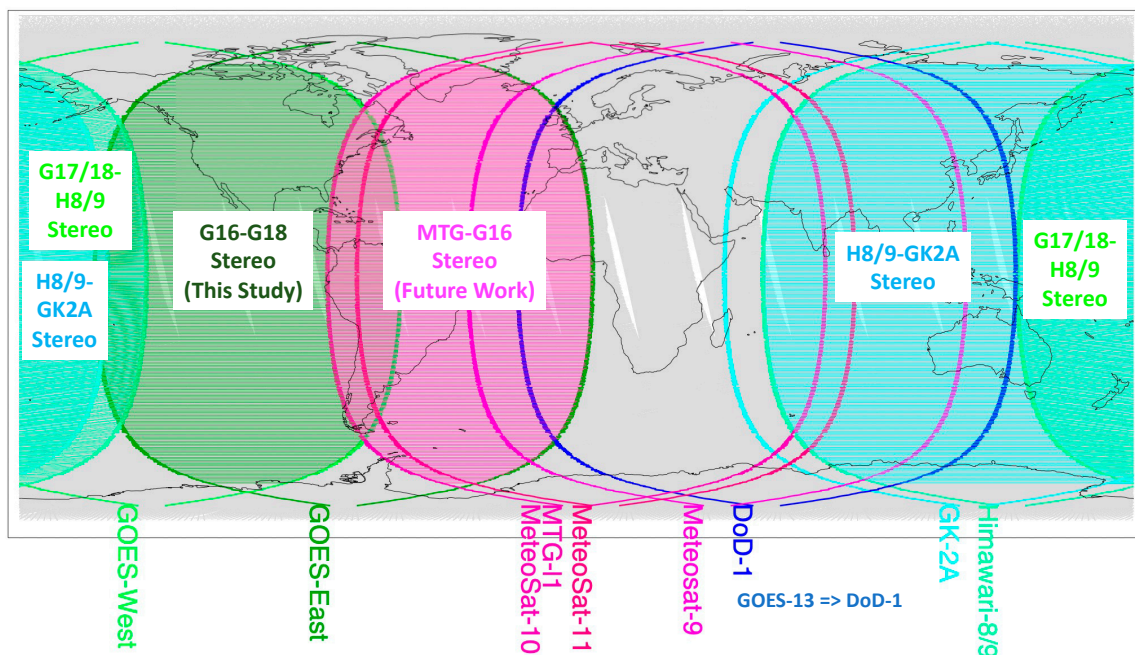

Figure 1. A schematic illustration of GEO-ring for current and future stereo observations (colored regions). The 3D-Wind algorithm has been developed and tested for the pairings of GOES/West (G17/G18) and GOES-East (G16), H8/H9–G17/G18, and is currently available for processing these data. The gray shaded swaths represent typical coverage from LEO satellites in which only the ascending orbits are used for illustration. A future development for GEO-GEO stereo will include the G16-MTG pairing to cover the Atlantic, South America, and West Africa regions.

The data used in this study come from the 11.2 μm (C14) imagery acquired by the Advanced Baseline Imager (ABI) on G18 and G16; G18 has been operational since 4 Jan

2023 as the GOES-West that is nominally stationed at 137.2°W, while G16 is nominally stationed at 75.2°W. Both satellites have a nearly identical set of 16-channel imagers and continue viewing Earth's Full Disk (FD) every 10 min. The GEO-GEO 3D-Wind algorithm and performance was detailed in [13]. We chose the TIR band C14 in this study to allow the continuous coverage of the overlapped region from the two imagers and enable the full diurnal cycle study of cloud dynamics. The C14 images from G16 and G18 have a pixel resolution of 2 km at the nadir. The stereo retrievals use a chip size of 24 × 24 pixels for pattern matching and a sampling spacing of 12 pixels.

As shown in Figure 2, the 3D-Wind algorithm produces a good yield for the stereo retrieval from the G16–G18 pairing on 1 February, especially over oceanic regions where clouds are ubiquitous. The typical uncertainty of wind and height retrievals are 0.2 m/s and 250 m from the GEO-GEO IR images [13]. A 5-day test study is used to distinguish between weather-driven and locally repeatable day-to-day variability, as several weather systems were swept through the domains of interest. In this study we focus on oceanic cloud dynamics and their diurnal variations and vertical distributions. For cloud height statistics, we normalized the cloud fraction by altitude (CfbA) or vertical probability density function (PDF), by the total number of stereo height measurements in each 10° × 10° (latitude–longitude) region. The size of the domains is chosen to have a sufficient number of samples for the PDF analysis. Time evolution of the PDF from these regions are tracked at every 10 min from 5 days of 3D-Wind retrievals.
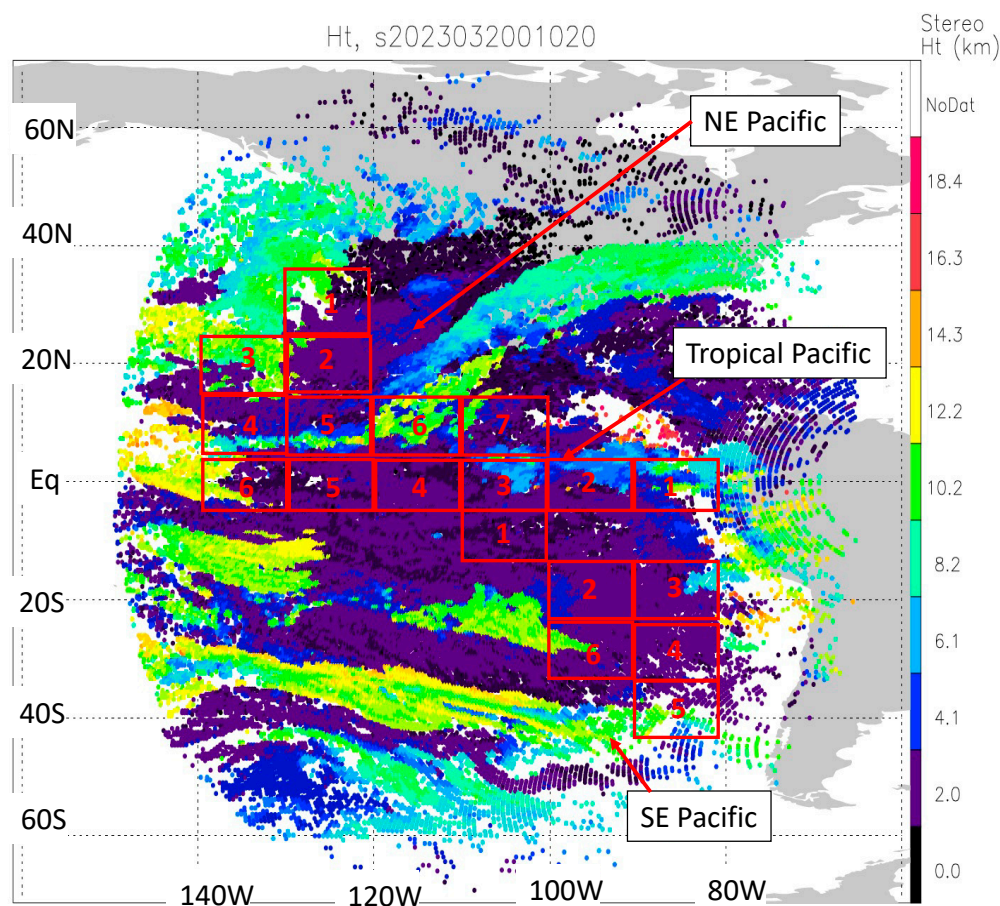

Figure 2. A frame of the G16–G18 stereo height retrieval on 1 February 2023 from the 3D-Wind algorithm. The red boxes indicate 10° × 10° (latitude–longitude) Pacific regions of interest in this study for tracking the diurnal variation. They are numbered and referred in the discussion, representing 6 tropical, 7 Northeast Pacific (NEP), and 6 Southeast Pacific (SEP) regions, and no data (NoDat) are indicated by the white. The tropical, NE Pacific, and SE Pacific regions are labeled by the number in each box to distinguish them from each other in the same latitude region.

Figure 3 provides an overview of the vertical distributions of CFbA and stereo winds acquired from 1–5 February 2023. These days were chosen only for the demonstration purpose since large data transfer from the archive would take a significant amount of time. The zonal mean statistics show a predominant presence of PBL clouds across all latitudes and upper-tropospheric clouds have a broad (~5 km) vertical distribution below the tropopause. One of the distinct features in the tropics is the congestus clouds that are difficult to observe with conventional IR height assignment methods [24]. A few cirrus clouds appeared in the tropical tropopause layer (TTL) during this 5-day period. The Eastern Pacific is a region that lacks deep convection, but extensive laminar cirrus can form from temperature perturbations induced by equatorially trapped Kelvin waves [25]. Compared to the Central and Western Pacific, the cirrus in the east occurs less frequently [26]. The diurnal cycle and interactions of these cloud systems now can be studied in detail using the 10 min stereo observations.
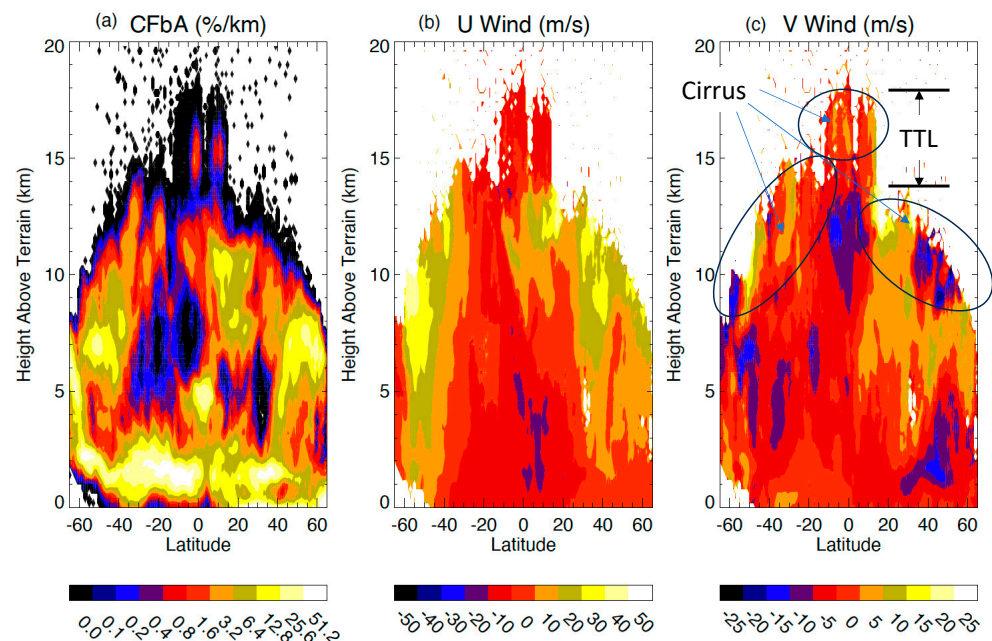

Figure 3. Zonal mean statistics for (**a**) cloud fraction by altitude (CFbA), (**b**) zonal (U) and (**c**) meridional (V) wind from the G16–G18 stereo retrievals on 1–5 February 2023. The latitude and height bins are 1° and 200 m, respectively. White color (NoDat) indicates "No Data". The nominal TTL and cirrus regions are denoted in the right panel.

3. Results

The 5-day stereo results from the G16–G18 pairing provided rich information on cloud dynamics and their diurnal variations over the Eastern Pacific. Here we selected a few interesting cases to illustrate these variations over the tropical and subtropical Pacific.

3.1. Tropical Clouds

Two tropical cloud cases are presented in Figures 4 and 5 to show the vertical distribution of predominant cloud systems and their time evolution. There are four major cloud types that are evident in both cases: PBL clouds (<2 km), altocumulus/congestus (3–6 km), convective outflows (8–11 km) and cirrus (14–17 km) [27]. Tropical cumulus clouds are dominated by shallow trade-wind cumulus, mid-level altocumulus/congestus, and deep cumulonimbus, which are well known as the trimodal distribution [28]. Convective outflows result from the deep convection that reaches the level of neutral buoyancy, extending impacts of deep convection to a wide area. In the (5°S–5°N, 110°W–100°W) region (Figure 4), the PBL clouds and altocumulus/congestus prevailed during the 5-day study period. Although CFbA has some day-to-day variability, diurnal variations of these

clouds are weak. A diurnal cycle is perhaps evident in CFbA at heights below 1 km. Meridional wind shears seem to play a significant role in these clouds, especially in the altocumulus/congestus, since the shears are present all the time. On 3 February the meridional wind shears appear to be stratiform, oscillating vertically in direction from the PBL to the tropopause. Over the 5-day period the upper-tropospheric clouds occur irregularly and come and go with any apparent correlation with the low clouds.

Figure 4. *Cont.*
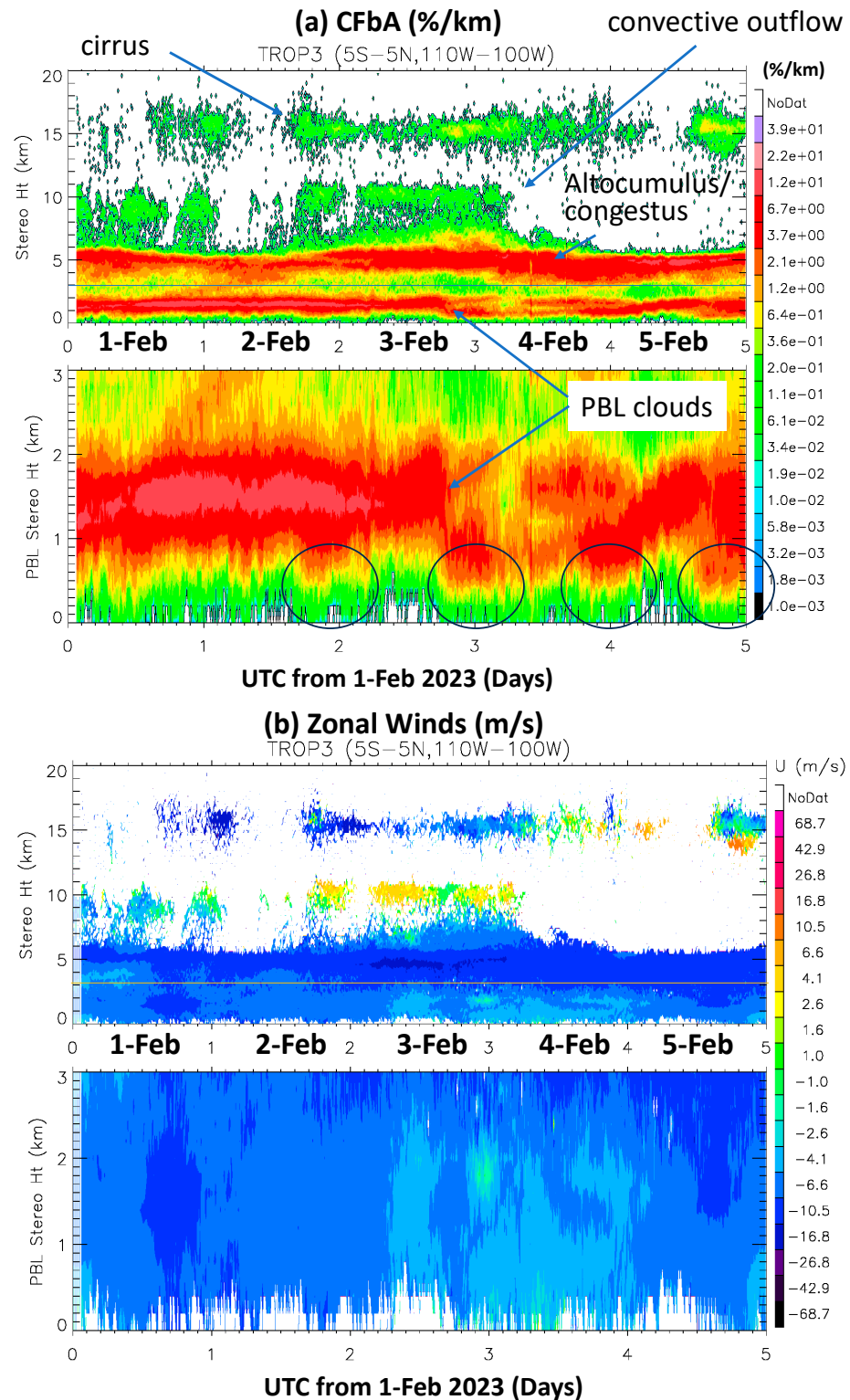
(c) Meridional Winds (m/s)
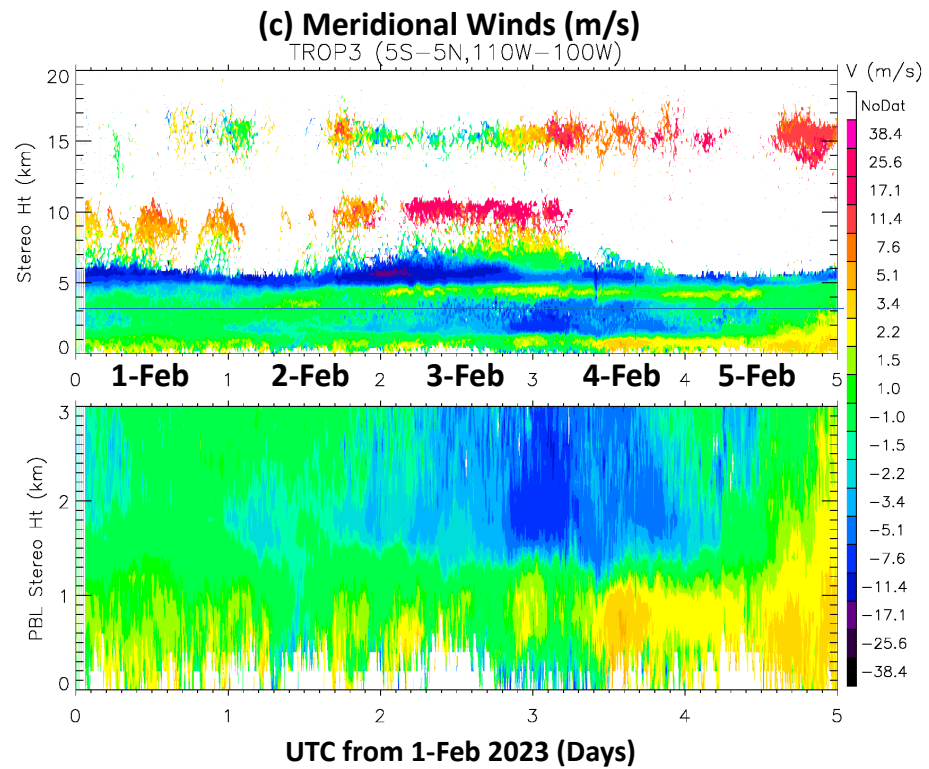
Figure 4. Time series of *the PDFs for* (**a**) stereo height, (**b**) zonal, and (**c**) meridional winds in the (5°S–5°N, 110°W–100°W) region. The data in the bottom panels are exactly the same as those in the top, but with an enlarged vertical scale to highlight the PBL variations at 0–3 km. The UTC (Coordinated Universal Time) in the plots starts from 1 February 2023.
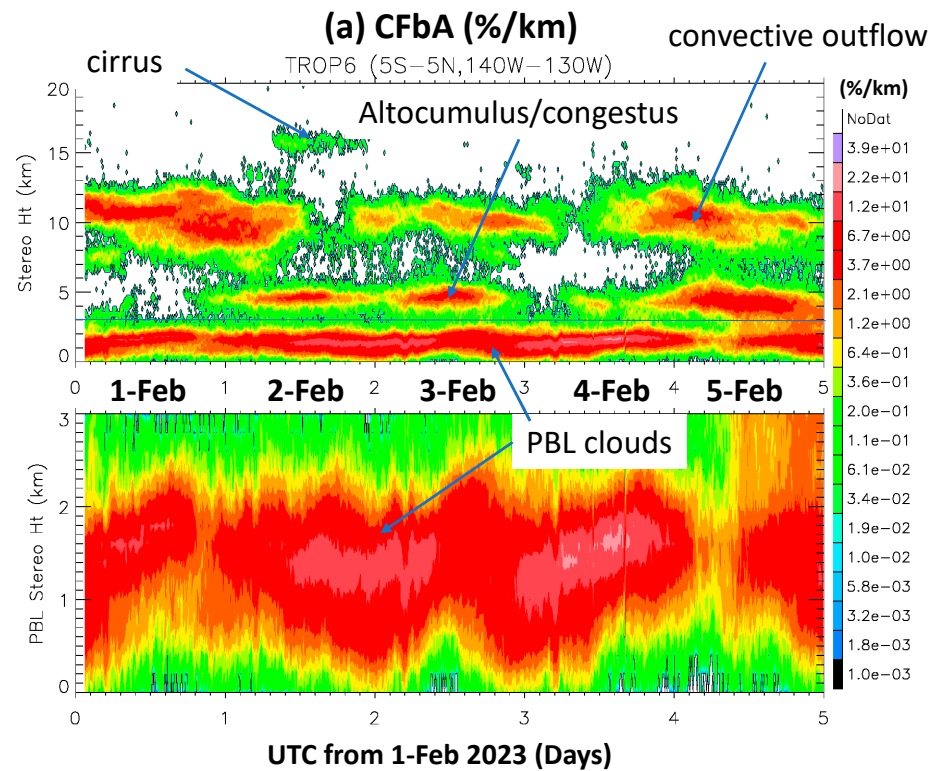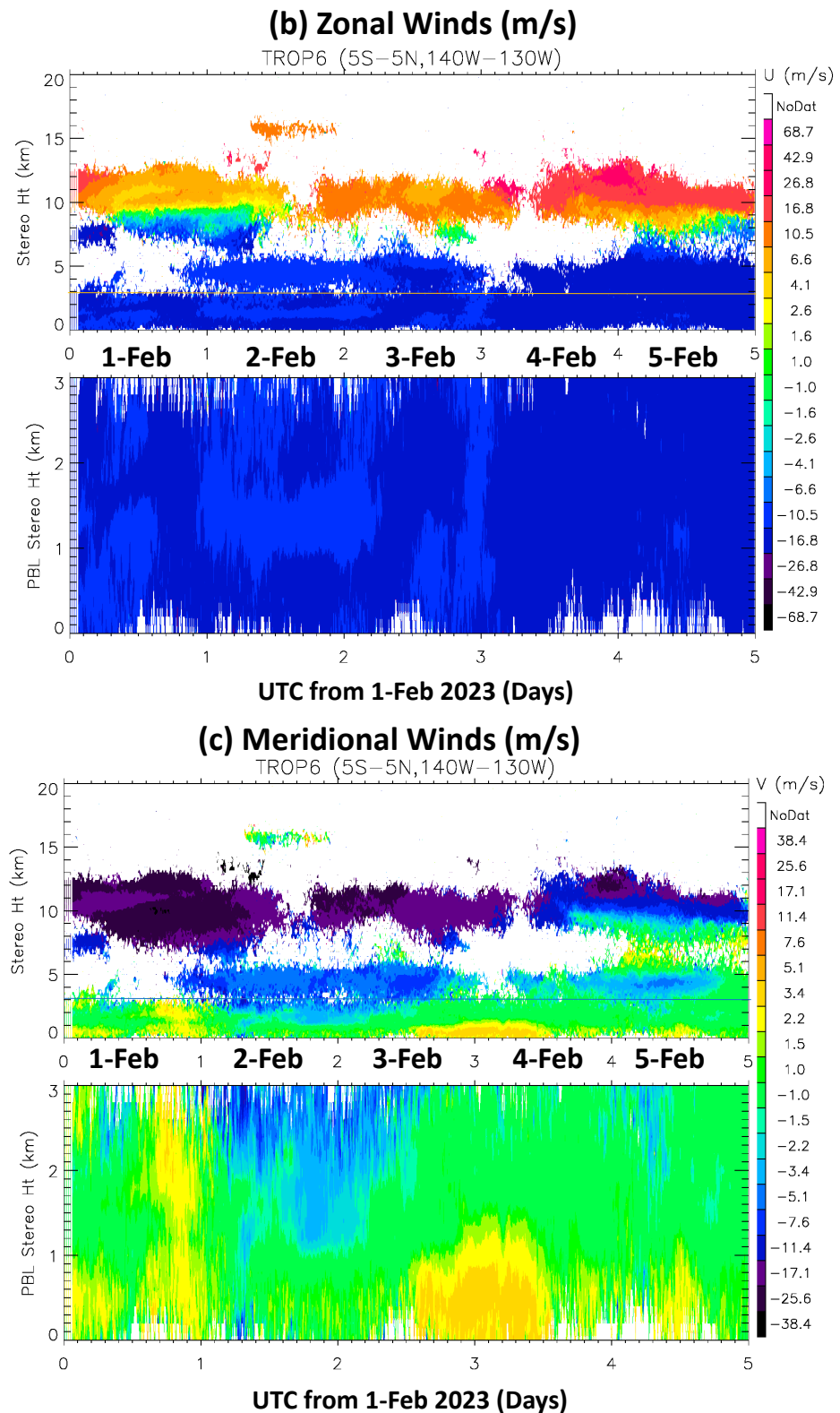
(a) CFbA (%/km)

Figure 5. *Cont.*

Figure 5. As in Figure 4 but for the (5°S–5°N, 140°W–130°W) region.

The tropical clouds in the (5°S–5°N, 140°W–130°W) region (Figure 5) reveal a slightly different morphology from those in Figure 4. The PBL clouds appear to have a quasi-two-day oscillation in CFbA, showing short periods of low cloudiness over the 5 days. These short periods seem to correlate well with the high clouds (i.e., convective outflows) at 8–12 km. The altocumulus/congestus variations are seen in concert with these periodic

cloud gaps in the PBL and upper troposphere. As in the previous tropical case, wind shears seem to play a role in these cloud variations, and strong zonal and meridional shears are evident on 1–2 and 4 February in the upper troposphere.

3.2. Subtropical Clouds

Two cases are selected to show cloud variations in the northern hemisphere (NH) and southern hemisphere (SH) subtropics where PBL is often cloudy and influenced by vertical wind shear. Over the NH subtropical (5°N–15°N, 110°W–100°W) region, cloud changes from 1 February to 5 February in this domain are seen in G18 imagery in the upper panels of Figure 6. However, stereo observations reveal more information on the cloud height evolution. As shown by CFbA in Figure 6, the low cloud system experiences a transition from the PBL-only to a double-layer (PBL and altocumulus/congestus). The mid-level winds appear to play a major role in forming the altocumulus/congestus layer, as a strong northward wind (3–5 m/s) is observed above the PBL clouds. A large wind shear began to occur within the PBL on 1 February, which led to a classic Ekman spiral (see next section).
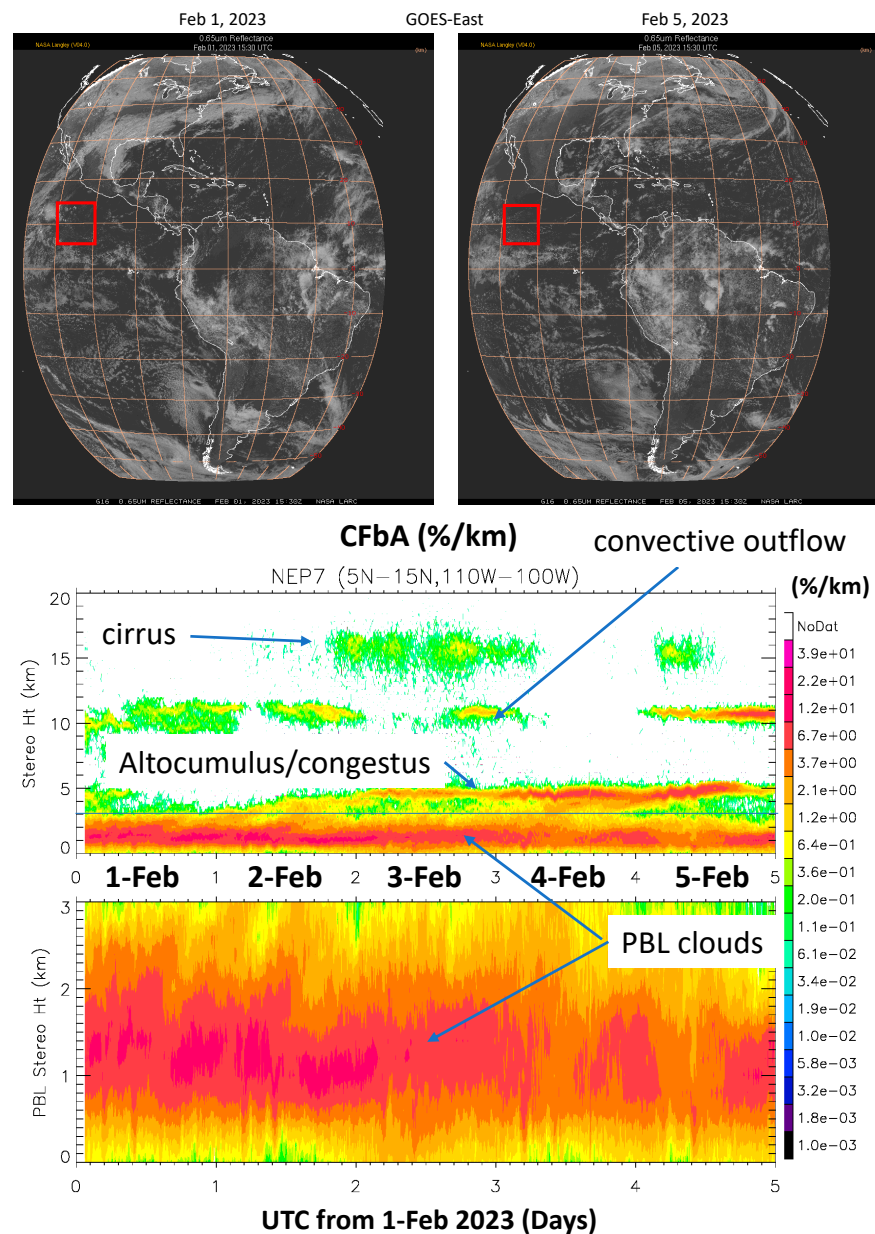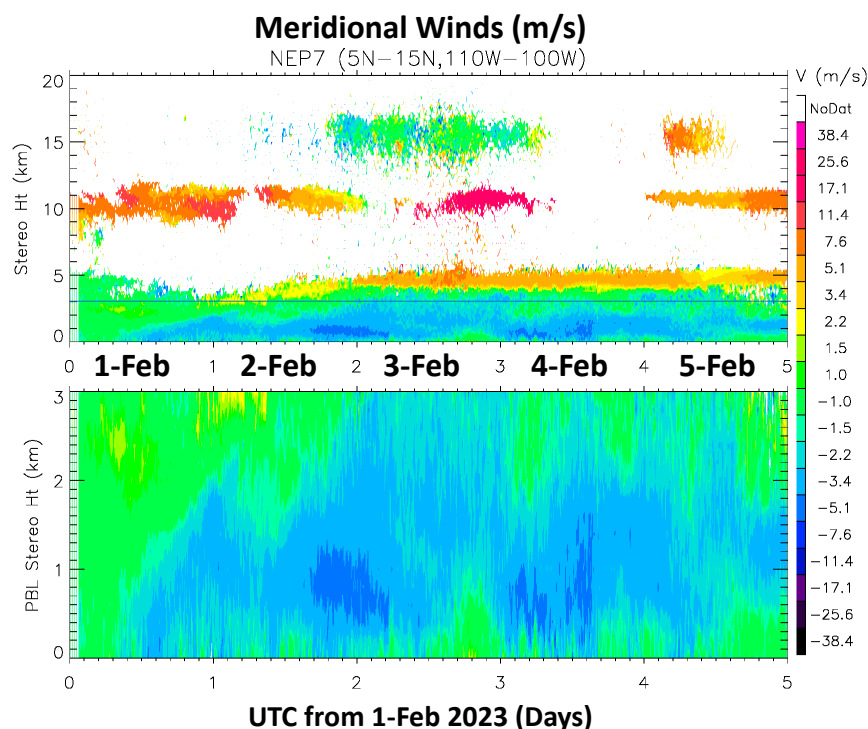

Figure 6. *Cont.*

Figure 6. Time series of CFbA and meridional (V) wind in the NH subtropical (5°N–15°N, 110°W–100°W) region. The upper panels are the GOES-East (G16) cloud images from 1 February and 5 February. The panels for CFbA and V have the same display as in Figure 3. GOES cloud images (last accessed on 21 March 2024 from https://satcorps.larc.nasa.gov/) are used to show the region of interest (red box) and cloud changes between 1 February and 5 February.

Figure 7 highlights the cloud variability in the SH subtropical (25°S–15°S, 100°W–90°W) region where the cloud system undergoes transition from stratocumulus (closed cell) to trade cumulus (open cell) clouds. Similarly, the G18 imagery from 1 February and 5 February are displayed in the upper panels without cloud height information. Because the bright stratocumulus over the SEP is very effective in reflecting the incoming solar radiation, their coverage and long lifetime have become an important research topic on cloud changes in a warmer climate. The G16–G18 stereo observations can track the evolution of these clouds at a 10 min interval. As seen in Figure 7, there is a strong diurnal variation in the closed-to-open cell transition. Around the 00Z UTC (or 17 h in local time), there are a significant number of clouds extended below 1 km, indicating more broken clouds or open cells. This is the period when precipitation occurs, which helps to remove some of the bright stratocumulus [29]. Unlike the NH subtropical case, the wind shears in this case play a minor role in the diurnal cycle of closed-to-open cell transition in the PBL. There is a clear diurnal cycle in the altocumulus/congestus clouds over this region during 1–3 February. Because the stereo algorithm can observe different cloud top heights in each $10° × 10°$ domain under a broken cloudy atmosphere, the vertical distribution of CFbA is indicative of how the clouds from different altitudes are related in this region. The appearance of altocumulus/congestus clouds (5–7 km) shows a lag, slightly behind the PBL clouds at a lower altitude (<1 km).
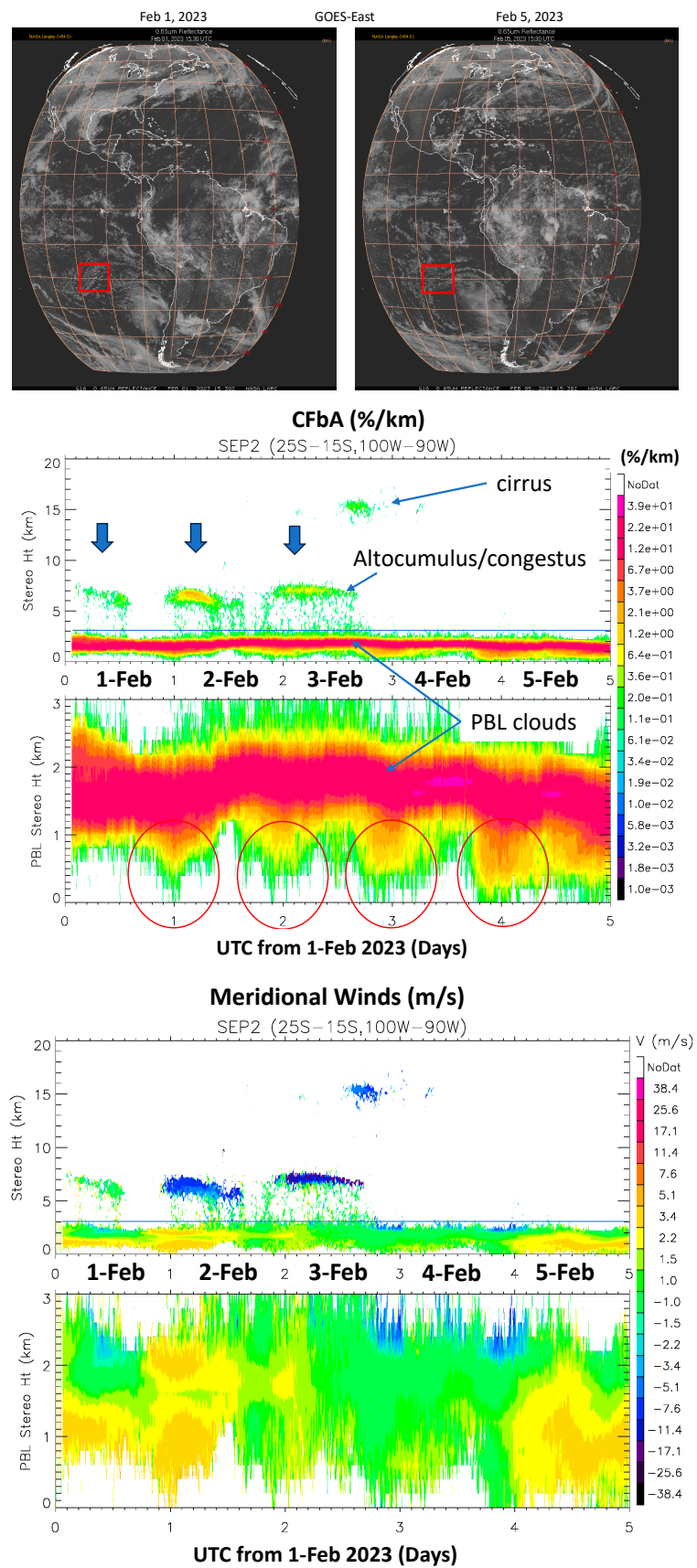
Figure 7. As in Figure 6 but for the SH subtropical (25°S–15°S, 100°W–90°W) region. The red cycles indicate the low-cloud occurrence extended to heights below 1 km near UTC~00Z, which corresponds to ~17 h in local time (LT) in this region.

3.3. Ekman Spirals in the PBL Stereo Winds

Spiral flows can occur in a shallow atmospheric/oceanic layer (aka, Ekman layer) near the surface where the viscous force and the Coriolis acceleration are the dominant forces in balance [30]. The viscous force, or friction in atmospheric flows, creates a vertical wind shear, which results in wind direction turning (aka Ekman spiral) by the Coriolis force as height increases. Although Ekman spirals can be readily observed from ground-based wind profilers, the PBL wind turning observations from space are rare, largely because it has been a challenge to resolve wind profiles with a sufficiently high vertical resolution.

Here, we report the first spaceborne observation of Ekman spirals from the 3D-Wind stereo technique. As shown in Figure 8, the 1 February mean winds in the two subtropical regions from the previous section reveal a wind direction turning with height as expected for the classic Ekman spiral. It shows a clockwise spiral in the NH subtropics and a counterclockwise spiral in the SH. In the 5-day G16–G18 stereo measurements, not all subtropical regions exhibit a spiral, nor in daily mean winds from other days in the two regions. As shown previously in Figures 6 and 7, the wind shears on 1 February were evolving slowly during the day, which allows daily mean winds to reveal the Ekman spiral. The wind turning phenomenon should be evident from the mean winds over a shorter period, but the 3D-Wind measurement noise would be larger.
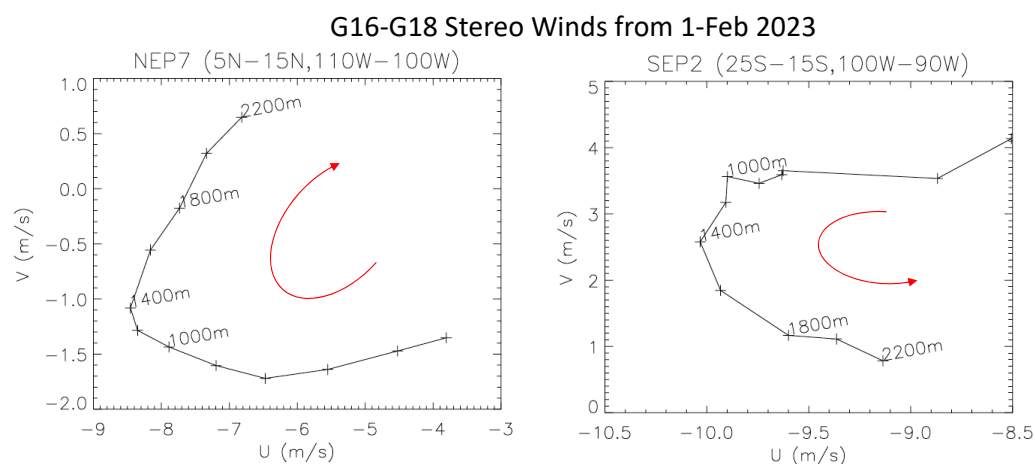

Figure 8. Hodograph of the daily (1 February) mean wind components as a function of height from the NH subtropical (5°N–15°N, 110°W–100°W) region (**left**) and the SH subtropical (25°S–15°S, 100°W–90°W) region (**right**). The height-dependent U–V relationship is known as the classic Ekman spiral as indicated by the red arrow.

To verify the Ekman spirals observed in the stereo winds, we compared the stereo observations with the ERA5 (European Centre for Medium-Range Weather Forecasts Reanalysis v5) data. Figure 9 shows the daily mean winds averaged over the same regions from 1 February. Although the mean wind values differ largely from the stereo winds, a wind turning spiral is evident in both regions, perhaps more pronounced in the NH subtropics. However, the amplitudes of the ERA5 spirals are smaller than the 3D-Wind observations in both cases. The observed Ekman spirals, a mesoscale process, have large day-to-day and region-to-region variations, which can pose a challenge to global models. In addition to model resolutions, the forcings that lead to the spirals need to be adequately represented in order for the spiral dynamics to occur. Figure 10 exhibits a transition in the PBL dynamics from a weaker to stronger zonal wind during 2–4 February, and the Ekman spiral nearly diminished on 3 February. Despite the similarity between the Ekman spirals in the ERA5 and the stereo observations, ship-based field campaigns with sounding profiles (e.g., radiosonde, Doppler lidars) will help to further validate these results.
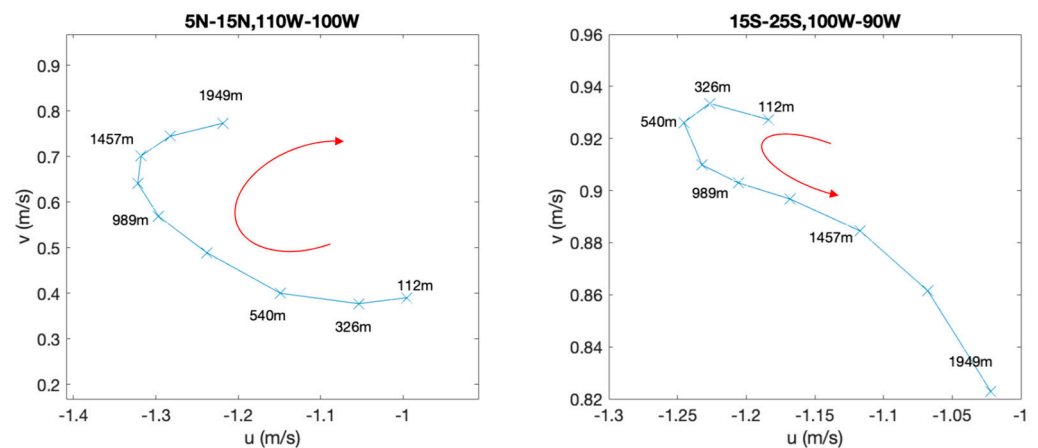
Figure 9. As in Figure 8 but from ERA5 daily mean winds (blue lines) over the same regions.
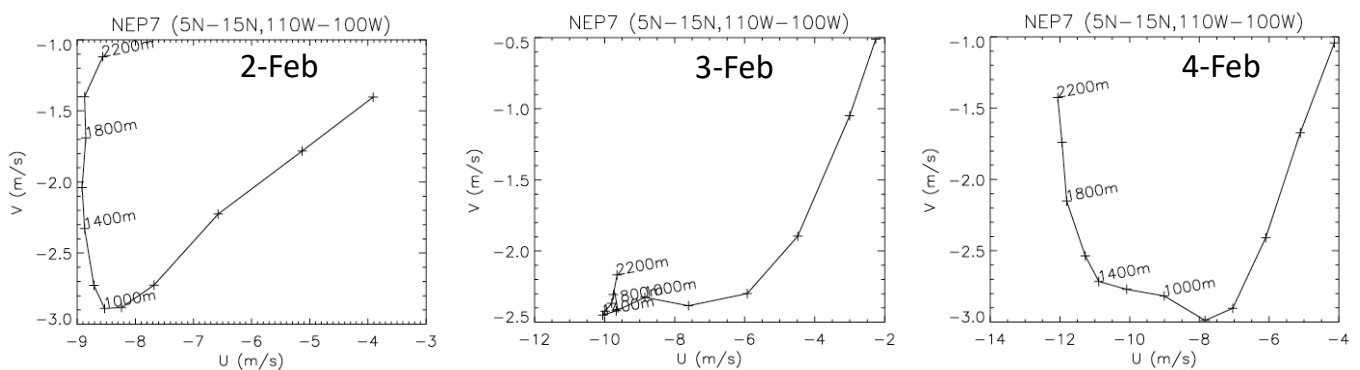

Figure 10. Day-to-day variations of the Ekman spiral from the same NEP regions in Figure 8 but continuing for 2–4 February. The winds at 1–2 km appear to change on 3 February with a stronger (weaker) zonal (meridional) component. The spire on 3 February is not as pronounced as the case on the other days.

4. Conclusions

GEO satellites can fully resolve the diurnal cycle over oceanic regions where atmospheric thermodynamics require a considerable amount of observational constraint, particularly in the PBL and the lower troposphere. It is challenging, however, for satellite remote sensing to measure PBL winds with a sufficient vertical resolution. The vertical resolution becomes even more important for better understanding and forecasting of adverse weather and pollutant transport in the PBL because of large variability in this region.

In this study we demonstrated the capability of a GEO-GEO stereo technique in observing the oceanic PBL winds and cloud structures as the dynamics evolve in this region. Using the newly-developed 3D-Wind algorithm, we retrieved stereo winds and cloud heights for five continuous days (1–5 February 2023) from the G16–G18 pairing over the Eastern Pacific, and featured several regional cases over a $10° \times 10°$ lat–lon domain. The structural evolution of cloud dynamics was tracked every 10 min in these regions. The improved vertical resolution from the stereo observations helps to resolve cloud layers with better detail compared to the cloud heights derived from the IR radiometric method. The cloud layers seen by the stereo retrieval in this period are: PBL clouds (<2 km), altocumulus/congestus (3–6 km), convective outflows (8–11 km) and cirrus (14–17 km). In addition, because of the sufficient vertical resolution with the stereo method, vertical wind shears can be observed and appear to play an important role in cloud formation.

The stereo winds and cloud heights are shown to be scientifically useful, especially for studying PBL dynamics and cloud variability. A strong diurnal variation is found over a SE Pacific region that is known as the transition zone from stratocumulus (closed cell) to trade cumulus (open cell) clouds. The diurnal cycle of PBL cloud occurrence appears to

correlate with precipitation around 17 h in local time, which is responsible for the broken stratocumulus at a lower level.

The good vertical resolution of the stereo technique allows to observe the classic Ekman spiral in the subtropical PBL. The NH (SH) subtropical spirals from 1 February mean winds show a clockwise (counterclockwise) wind direction change with height, as expected for the typical air flow in the Ekman layer. With the advanced spatiotemporal sampling from GEO-GEO stereo AMVs, it may be enlightening to carry out a comprehensive analysis for the statistical properties (e.g., distribution and duration) of these spirals over the Eastern Pacific.

References

1. Shepherd, T.G. Atmospheric circulation as a source of uncertainty in climate change projections. *Nat. Geosci.* **2014**, *7*, 703–708. [CrossRef]
2. Whitehead, V.S.; Browne, I.D.; Garcia, J.G. Cloud height contouring from Apollo 6 photography. *Bull. Amer. Meteor. Soc.* **1969**, *50*, 522–528. [CrossRef]
3. Minzner, R.A.; Shenk, W.E.; Teagle, R.D.; Steranka, J. Stereographic cloud heights from imagery of SMS/GOES satellites. *Geophys. Res. Lett.* **1978**, *5*, 21–24. [CrossRef]
4. Hasler, A.F. Stereographic observations from geosynchronous satellites: An important new tool for the atmospheric sciences. *Bull. Amer. Meteor. Soc.* **1981**, *62*, 194–212. [CrossRef]
5. Takashima, T.; Takayama, Y.; Matsuura, K.; Naito, K. Cloud Height Determination By Satellite Stereography. *Pap. Meteorol. Geophys.* **1982**, *33*, 65–78. [CrossRef]
6. Lorenz, D. Stereoscopic imaging from polar orbit and synthetic stereo imaging. *Adv. Space Res.* **1983**, *2*, 133–136. [CrossRef]
7. Fujita, T.T.; Dodge, J.C. Applications of stereoscopic height computations from dual geosynchronous satellite data/joint NASA–Japan stereo project. *Adv. Space Res.* **1983**, *2*, 153–160. [CrossRef]
8. Mack, R.; Hasler, A.F.; Rodgers, E.B. Stereoscopic observations of hurricanes and tornadic thunderstorms from geosynchronous satellites. *Adv. Space Res.* **1983**, *2*, 143–151. [CrossRef]
9. Lancaster, R.S.; Spinhirne, J.D.; Manizade, K.F. Combined infrared stereo and laser ranging cloud measurements from shuttle mission STS–85. *J. Atmos. Ocean. Technol.* **2003**, *20*, 67–78. [CrossRef]
10. Frey, R.A.; Baum, B.A.; Menzel, W.P.; Ackerman, S.A.; Moeller, C.C.; Spinhirne, J.D. A comparison of cloud top heights computed from airborne lidar and MAS radiance data using CO_2 slicing. *J. Geophys. Res. Atmos.* **1999**, *104*, 24547–24555. [CrossRef]
11. Carr, J.L.; Wu, D.L.; Kelly, M.A.; Gong, J. MISR-GOES 3D Winds: Implications for Future LEO-GEO and LEO-LEO Winds. *Remote Sens.* **2018**, *10*, 1885. [CrossRef]
12. Carr, J.L.; Wu, D.L.; Wolfe, R.E.; Madani, H.; Lin, G.G.; Tan, B. Joint 3D-Wind Retrievals with Stereoscopic Views from MODIS and GOES. *Remote Sens.* **2019**, *11*, 2100. [CrossRef]
13. Carr, J.L.; Wu, D.L.; Daniels, J.; Friberg, M.D.; Bresky, W.; Madani, H. GEO–GEO Stereo-Tracking of Atmospheric Motion Vectors (AMVs) from the Geostationary Ring. *Remote Sens.* **2020**, *12*, 3779. [CrossRef]
14. Carr, J.L.; Horváth, Á.; Wu, D.L.; Friberg, M.D. Stereo plume height and motion retrievals for the record-setting Hunga Tonga-Hunga Ha'apai eruption of 15 January 2022. *Geophys. Res. Lett.* **2022**, *49*, e2022GL098131. [CrossRef]
15. Carr, J.L.; Wu, D.L.; Friberg, M.D.; Summers, T.C. Multi-LEO Satellite Stereo Winds. *Remote Sens.* **2023**, *15*, 2154. [CrossRef]

16. Kelly, G.; Thepaut, J.-N.; Buizza, R.; Cardinali, C. The value of observations. *I: Data denial experiments for the Atlantic and Pacific. Quart. J. Roy. Meteor. Soc.* **2007**, *133*, 1803–1815.
17. Gelaro, R.; Langland, R.H.; Pellerin, S.; Todling, R. The THORPEX observation impact inter-comparison experiment. *Mon. Weather Rev.* **2010**, *138*, 4009–4025. [CrossRef]
18. Chapel, J.; Stancliffe, D.; Bevacqua, T.; Winkler, S.; Clapp, B.; Rood, T.; Gaylor, D.; Freesland, D.; Krimchansky, A. Guidance, navigation, and control performance for the GOES-R spacecraft. *CEAS Space J.* **2015**, *7*, 87–104. [CrossRef]
19. Tan, B.; Dellomo, J.J.; Folley, C.N.; Grycewicz, T.J.; Houchin, S.; Isaacson, P.J.; Johnson, P.D.; Porter, B.C.; Reth, A.D.; Thiyanaratnam, P.; et al. GOES-R series image navigation and registration performance assessment tool set. *J. Appl. Remote Sens.* **2020**, *14*, 032405. [CrossRef]
20. Stone, R.E.; Pauley, P.; Christophersen, H.; Reeves, J. Evaluation of Dual Geostationary Stereo Winds in NAVGEM. In Proceedings of the 16th International Winds Workshop (IWW16), Montréal, QU, Canada, 8–12 May 2023.
21. Horváth, Á.; Bresky, W.; Daniels, J.; Vogelzang, J.; Stoffelen, A.; Carr, J.L.; Wu, D.L. Evolution of an atmospheric Kármán vortex street from high-resolution satellite winds: Guadalupe Island case study. *J. Geophys. Res. Atmos.* **2020**, *125*, e2019JD032121. [CrossRef]
22. Carr, J.L.; Daniels, J.; Wu, D.; Bresky, W.; Madani, H.; Friberg, M.; Summers, T. Advances in Stereo Winds. In Proceedings of the 16th International Winds Workshop, Montréal, QU, Canada, 8–12 May 2023.
23. Carr, J.L.; Daniels, J.; Wu, D.L.; Bresky, W.; Tan, B.A. Demonstration of Three-Satellite Stereo Winds. *Remote Sens.* **2022**, *14*, 5290. [CrossRef]
24. Wu, D.L.; Ackerman, S.A.; Davies, R.; Diner, D.J.; Garay, M.J.; Kahn, B.H.; Maddux, B.C.; Moroney, C.M.; Stephens, G.L.; Veefkind, J.P.; et al. Vertical distributions and relationships of cloud occurrence frequency as observed by MISR, AIRS, MODIS, OMI, CALIPSO, and CloudSat. *Geophys. Res. Lett.* **2009**, *36*. [CrossRef]
25. Taylor, J.R.; Randel, W.J.; Jensen, E.J. Cirrus cloud-temperature interactions in the tropical tropopause layer: A case study. *Atmos. Chem. Phys.* **2011**, *11*, 10085–10095. [CrossRef]
26. Wang, T.; Wu, D.L.; Gong, J.; Tsai, V. Tropopause laminar cirrus and its role in the lower stratosphere total water budget. *J. Geophys. Res. Atmos.* **2019**, *124*, 7034–7052. [CrossRef]
27. Wallace, J.M.; Hobbs, P.V. *Atmospheric Science: An Introductory Survey*; Academic Press: Cambridge, MA, USA, 2006; Volume 92.
28. Johnson, R.H.; Rickenbach, T.M.; Rutledge, S.A.; Ciesielski, P.E.; Schubert, W.H. Trimodal characteristics of tropical convection. *J. Clim.* **1999**, *12*, 2397–2418. [CrossRef]
29. Wood, R. Stratocumulus clouds. Review paper. *Mon. Weather Rev.* **2012**, *140*, 2373–2423. [CrossRef]
30. Ekman, V.W. On the influence of the Earth's rotation on ocean currents. *Arch. Math. Astron. Phys.* **1905**, *2*, 1–52.